

Understanding Onsager Phenomenological Matrix of Interfacial Friction and Heat
Transfer in Graphene Nanochannels

Cheng Gao

Dept. of Chemistry, University of California, Berkeley

A thesis submitted in partial fulfillment of the requirements for the degree of
Bachelor of Science with Honors in Chemistry, under the supervision of
Professor David Limmer

Professor David Limmer

Spring 2019

Abstract

Graphene possesses an exceptional high slip length due to its atomically smooth surface and strong covalent bonding framework, making graphene an ideal material for constructing nanofluidic devices. Nevertheless, shearing flow generates heat and complicate the environment at the microscopic scale. In this thesis, I reviewed two popular equilibrium methods to calculate friction coefficient and highlighted assumptions often overlooked in derivations and practicality concerning implementation of a carbon nanochannel. The dependence of friction coefficients on a variety of parameters were discussed. Moreover, in-plane and out-plane heat transfer coefficients were studied via a Green-Kubo relations. Lastly, the correlation between friction and heat were considered within the formalism of Onsager reciprocal relation and computed by a cross correlation function. Nonequilibrium molecular dynamics was also used extensively to verify equilibrium results.

Table of Contents

Acknowledgement.....	ii
1 Introduction.....	1
2 Relevant Concepts in Statistical Mechanics.....	3
2.1 Basics of numerical simulation.....	3
2.1.1 Ergodic hypothesis.....	3
2.1.2 Langevin dynamics.....	4
2.2 Linear response.....	6
2.2.1 Static linear response theory.....	6
2.2.2 Classical time correlation function.....	7
2.2.3 Time-dependent linear response.....	7
2.3 Basic fluid mechanics.....	6
3 Interfacial Friction Coefficient.....	10
3.1 Theory of equilibrium methods.....	10
3.1.1 Bocquet and Barrat method.....	10
3.1.2 Hansen method.....	11
3.2 Equilibrium simulations and results.....	14
3.2.1 System setup.....	14
3.2.2 Basic results of the two methods.....	15
3.2.3 Dependence of friction coefficient on wall thermostat.....	16
3.2.4 Dependence of friction coefficient on sheet flexibility	17
3.2.5 Dependence of friction coefficient on slab width.....	18
3.2.6 Dependence of friction coefficient on length of wall.....	18
3.2.7 Dependence of friction coefficient on channel width.....	19
3.2 Nonequilibrium simulations and results.....	20
3.3.1 Density profiles.....	20
3.3.2 Velocity profiles.....	21
3.3.3 Dependence of friction coefficient on channel width.....	21
4 Heat Transfer Coefficient.....	23
4.1 Equilibrium methods and results.....	23
4.2 Nonequilibrium methods and results.....	25
4.3 Correlation between friction and heat current.....	26
4.3.1 Onsager reciprocal relation.....	26
4.3.2 Cross correlation function.....	28
4.3.3 Heat generated from channel flow.....	29
Conclusion and Outlooks.....	30
Bibliography.....	31

Acknowledgement

First of all, I would not have come to UC Berkeley without my mother, Lydia Lee, who took care of me in my most troublesome years. My mother's success as an immigrant businesswoman serves as a constant source of inspiration. I would also like to thank the financial support from my father, Jinbo Gao, for college which enables me to focus on learning.

I am hugely indebted to Professor David Limmer who gave me a chance to start learning and doing research in statistical mechanics. I appreciate Chloe Gao for being one of the most knowledgeable, and patient mentors who not only provided constant feedback and suggestions for my research project but also helped me enjoy CHEM220B. I also want to express my esteem for Avishek Das who carried me through CHEM221A and gave me additional insights on my research project. In addition, I want to thank Trevor Grand Pre and Ben Kuznets-Speck for being great office mates and Mirza Galib, Samuel Niblett, Addison Schile, Yoojae Park, Amael Obliger, Laura Scalfi, and Shujiang Liang for creating a supportive and fun working environment.

My undergraduate experience would not have been great without Chris Chi, Sophia Weng, and Wesley Wang. Moreover, I would love to thank Maura Daly, Joelle Martin and Aayush Patel for making ChemScholar sections my most cherished moments. Most importantly, I want to appreciate my girlfriend, Yushi Yan, for supplying uncountable amount of happiness and courage.

Chapter 1

Introduction

Both organic and inorganic carbon compounds have been studied extensively since the birth of modern chemistry. The elemental allotropes such as graphite and diamond have also been applied in many industrial and scientific settings. Although scientists understood that a two-dimensional carbon allotrope existed, graphene, a single layer of carbon atoms arranged in a hexagonal lattice, could not be extracted until 2004 when Andre Geim and Kostya Novoselov at University of Manchester realized the a single layer of graphite can be isolating by applying sticky tape on the surface of graphite[1].

In popular culture, graphene is widely recognized for its exceptional flexibility and applicability in developing wearable electronics and bendable screens[2]. A less publicly aware property of graphene is its large slip length which is crucial for developing nanofluidics devices such as nano-mechanical systems, nanobiosensors and lab-on-a-chip. These devices have the potential to improve the efficiency of water desalination and the potency of drug delivery[3-4].

The no-slip boundary condition which states-at a solid boundary, the fluid will have zero velocity relative to the boundary-has always been assumed at the macroscopic scale. However, for systems at the microscopic scale, the molecular interactions at the liquid-solid boundary becomes pronounced, giving rise to a slip length, an extrapolated distance relative to the solid boundary where the tangential velocity component vanishes. Slip length is positively correlated with the density of fluid and wall, contact angle, viscosity and temperature; slip length is negatively correlated with the attractions between fluid and wall[5]. Usually, the interaction among the fluid molecules are stronger than interactions between the fluid and graphene surface. The surface density of graphene is also much higher than the density of liquid. In addition, the covalent network ensures the surface of graphene is smooth[6]. All of these three characteristics suggest that graphene is capable of having a large slip length.

Just as slip length becomes non-negligible at the length scale of a few nm, finite size effects must be taken into consideration. Finite size scaling, or how a transport coefficient differs when the size of the system is tuned in this context, is particularly challenging and interesting. Previous researchers have shown the geometries of confinements and the scaling of transport coefficients are intrinsically linked[7]. However, the focus of this research is on graphene nanochannel.

Graphene also possesses extraordinary in-plane heat conductivity due to covalent sp^2 bonding between carbon atoms, making graphene a good candidate for transistors. However, out-of-plane heat flow is limited by weak van der Waals interactions[8]. The lack of ability to transfer heat out-of-plane may introduce complications in nanofluidics devices as optimal transport conditions may have delicate dependence on temperature; for instance, a microreactor often demands a specific range of temperature for the chemical reaction to proceed[4]. Therefore, in order to produce manageable and high-quality nanofluidic devices, a concrete understanding on the transport phenomena at the graphene-liquid interface is necessary. Although both friction and heat transfer coefficients have been studied independently, the connection between them remains to be elucidated.

The organization of this thesis is as follows. First in Chapter 2, a review of basic concepts on statistical mechanics and fluid mechanics is provided. In Chapter 3, a comparison of two approaches of obtaining friction coefficient at equilibrium is discussed in tandem with direct non-equilibrium method. Furthermore, the effect on friction coefficient with respect to change of the aspect ratio of graphene nanochannel is considered. In Chapter 4, heat transfer coefficient at liquid-solid interface and its connection with friction are discussed. Moreover, the correlation between friction and the heat was studied via the formalism of Onsager reciprocal relation.

Chapter 2

Relevant Concepts in Statistical Mechanics

This chapter aims to address basic concepts in statistical mechanics commonly taught in first year graduate level courses. Particularly, the following sections are primarily based on Chem220B taught at UC Berkeley[9]. First a short discussion on the ergodic hypothesis is provided. Then, the idea and limiting behavior of Langevin equations and how a simulated system can be propagated through time is discussed. Next, time-dependent linear response theory and Green-Kubo relations are reviewed. Lastly, boundary conditions of shear flow are discussed.

2.1 Basics of numerical simulation

2.1.1 Ergodic hypothesis

For interacting systems away from phase coexistence, the time spent by a simulation trajectory in some region of the phase space with the same energy is proportional to the hypervolume of this region; in other words, the time average of a physical property \bar{A} in the long time limit is equal to the ensemble average of the property $\langle A \rangle$,

$$\bar{A} = \lim_{t_{obs} \rightarrow \infty} \frac{1}{t_{obs}} \int_0^{t_{obs}} dt A(t) \quad (2.1)$$

$$\langle A \rangle = \int dq^N \int dp^N A \rho(q^N, p^N) \quad (2.2)$$

$$\bar{A} = \langle A \rangle \quad (2.3)$$

where t_{obs} is the observation time, p and q are dynamical variables and ρ is the probability density. This assumption, known as the ergodic hypothesis, justifies the use of numerical simulation to study dynamical behavior of a physical system. Although the idea of ergodicity appears to be closely related with the microcanonical ensemble, ergodicity applies to both canonical and grand canonical ensemble because of ensemble equivalency. In a canonical ensemble, the probability density is simply the Boltzmann distribution. Moreover, ergodicity also applies to most of nonequilibrium steady states. Because the derivation for this extension is extremely complicated, readers are referred to external sources for a rigorous mathematical justification [10].

From a practical perspective, ensemble averages are not always analytically solvable. Therefore, obtaining accurate time averages become important. Convergence of time averages of a time-independent physical property such as transport coefficients indicates the system in a given ensemble has been sufficiently sampled.

2.1.2 Langevin dynamics

In a canonical ensemble, a system is coupled to an external bath and is able to exchange energy with it. If one assumes the bath is composed of harmonic oscillators, then the generalized Langevin equation describes the motion of particles in the system,

$$m\ddot{x} = -w'(x) - 2 \int_0^t dt' \gamma(t-t')\dot{x} + R(t) \quad (2.4)$$

$$\langle R(t)R(t') \rangle = 2k_B T \gamma(t-t') \quad (2.5)$$

where $w(x)$ is the potential energy averaged over the bath, $\gamma(t)$ is a response function encoding the history of the bath, and $R(t)$ is a random force that exactly balances the friction. In numerical simulation, the Langevin equation serves as a thermostat to ensure the system can relax to equilibrium, allowing the canonical distribution to be sampled.

If the bath is assumed to relax very quickly relative to the system, or Markovian, the generalized Langevin equation can be simplified to

$$\gamma(t) = \gamma\delta(t) \quad (2.6)$$

$$m\ddot{x} = -w'(t) - \gamma\dot{x}(t) + R(t) \quad (2.7)$$

Note γ has the physical dimension of $\frac{\text{mass}}{\text{time}}$. In implementation of this underdamped limit, γ is often rewritten as

$$\gamma = \frac{m}{\tau} \quad (2.8)$$

where τ is the characteristic relaxation time of the bath and this equation is applied on a per-particle basis.

In practice, tracking the full history of bath is impractical. Consider the case where $\gamma \gg 0$. Due to overwhelming friction, inertia becomes insignificant, and the equation of motion is simplified to

$$\gamma \dot{x}(t) = -w'(x) + R(t) \quad (2.9)$$

known as the overdamped Langevin equation, or Brownian motion. Throughout this project, an underdamped Langevin equation was used whenever a Langevin thermostat is applied.

2.2 Linear response

Linear response theory is very useful for treating both classical and quantum mechanical systems. However, in this section, the focus is on time-dependent classical linear response theory and how the idea is connected to transport coefficients and equilibrium dynamics.

2.2.1 Static linear response theory

Consider a small perturbation conjugate to the dynamical variable q , the Hamiltonian of the system can be written as,

$$H = H_0(q) - Fq \quad (2.10)$$

where $H_0(q)$ is the Hamiltonian of the equilibrium system. Then average of q in the perturbed ensemble, $\langle q \rangle_F$ is

$$\langle q \rangle_F = \frac{\int dq^N \int dp^N q e^{-\beta[H_0(q)-Fq]}}{\int dq^N \int dp^N e^{-\beta[H_0(q)-Fq]}} \quad (2.11)$$

Assume F is small and the Taylor expansion of $e^{\beta Fq}$ to first order yields,

$$\langle q \rangle_F = \frac{\langle q \rangle_0 + \beta F \langle q^2 \rangle_0}{1 + \beta F \langle q \rangle_0} \quad (2.12)$$

Where $\langle \cdot \rangle_0$ denotes an equilibrium average. Again use Taylor expansion on $\frac{1}{1 + \beta F \langle q \rangle_0}$ to the first order and obtain

$$\langle q \rangle_F \approx \langle q \rangle_0 + \beta F \langle (\delta q)^2 \rangle_0 + \mathcal{O}(F^2) \quad (2.13)$$

Depending on the truncation of the first Taylor expansion, this approach can be extended to many orders. For example, the second order response is

$$\langle q \rangle_F \approx \langle q \rangle_0 + \beta F \langle (\delta q)^2 \rangle_0 + \frac{\beta^2 F^2}{2} \langle (\delta q)^3 \rangle_0 \quad (2.14)$$

Clearly, the beauty of this theory arises from the structure that an arbitrary forced system can be described by the cumulants of a biased variable in a reference system.

2.2.2 Classical time correlation function

At the microscopic scale, equilibrium is dynamic so time correlation functions are useful tools to infer dynamical information. Time correlation functions are defined as

$$C_{AB}(t_1, t_2) = \langle A(t_1)B(t_2) \rangle \quad (2.15)$$

$$= \int dq^N \int dp^N A(q, p, t_1)B(q, p, t_2)f_0(q, p) \quad (2.16)$$

where A and B are operators on phase space and have a nontrivial time dependence, and f_0 is the stationary distribution. When $A = B$, the correlation function is known as the autocorrelation function; when $A \neq B$, the correlation function is called the cross correlation function.

Classical equilibrium correlation functions have a few properties worth mentioning. The most fundamental property is stationarity,

$$C_{AB}(t_1, t_2) = C_{AB}(t_1 - t_2, 0) \quad (2.17)$$

which can be derived from the anti-self-joint property of the Liouvillian.

Classical time correlation functions can have both odd and even symmetry with respect to time reversal because signs of time and direction of momenta are inverted for a classical equation of motion. Therefore, observables with explicit position dependence are even in time. Autocorrelation functions are even in time,

$$C_{AA}(t) = C_{AA}(-t) \quad (2.18)$$

Moreover, if mix observables have dependence on both position and momenta, the correlation function are odd in time,

$$\langle A(p, 0)B(q, t_2) \rangle = -\langle A(p, 0)B(q, -t_2) \rangle \quad (2.19)$$

2.2.3 Time-dependent linear response

Again consider a small perturbation $-Fq$ to the system, q at a given time t averaged over initial conditions is

$$\bar{q}(t) = \frac{\int dq^N \int dp^N q(t) e^{-\beta[H_0(q) - Fq]}}{\int dq^N \int dp^N e^{-\beta[H_0(q) - Fq]}} \quad (2.20)$$

Apply a Taylor expansion to the first order in F as in the static case to obtain,

$$\bar{q}(t) = \langle q(t) \rangle_0 + \beta F \langle \delta q(0) \delta q(t) \rangle_0 \quad (2.21)$$

$$= \langle q \rangle_0 + \beta F C_{qq} \quad (2.22)$$

where the second term on the right side contains a time correlation function of deviations of the dynamical variable.

A system where a small perturbation applies is in the linear response regime and transport coefficients describes how rapidly this system relaxes back to equilibrium. Linear

transport coefficients are closely related with time correlation functions through Green-Kubo relations,

$$D \propto \beta F \int_0^\infty \langle \dot{A}(0) \dot{A}(t) \rangle_{F=0} dt \quad (2.23)$$

where \propto is used to indicate that transport coefficients are often normalized to be independent of system size. Moreover, if the observables are isotropic, generalized Einstein relation also describes linear transport coefficients,

$$2Dt = \langle |A(t) - A(0)|^2 \rangle \quad (2.24)$$

And a close relation between correlation functions of time derivative of an observable and its mean squared difference is recognized. In practice, if one approach is too noisy, using the other approach may alleviate the problem. Green-Kubo relation will be used throughout this thesis and the proofs for friction coefficient and heat transfer coefficient will be provided in Chapter 3 and 4, respectively.

2.3 Basic fluid mechanics

At length scales of a few nanometers, slip length become visible and generalized boundary conditions are necessary to describe the physics at the interface. The general boundary condition is

$$u_s = L_s \frac{\partial u_x}{\partial y} \Big|_{y=y_w} \quad (2.25)$$

which assumes x is the direction of flow and y is the direction of confinement. u_s is the slip velocity defined as the relative tangential velocity between the fluid and the solid, L_s is the slip length, and the partial derivative term is the strain rate evaluated at the boundary. At the microscopic scale, the excluded volume between wall and fluid and the layered feature of fluid become visible so y_w is often chosen as the first peak in density near the wall. This boundary is crucial for inferring slip length from a non equilibrium simulation as strain rate and slip velocity can be directly obtained from a velocity profile. Poiseuille flow is a simple but realistic model non equilibrium system where a constant force is applied to the liquid. In this case, a parabolic velocity profile with peak at the center ($y=0$) is observed.

$$u_x(y) = ay^2 + c \quad (2.26)$$

$$\frac{\partial u_x}{\partial y} \Big|_{y=y_w} = 2ay_w \quad (2.27)$$

where a and c are fitting parameters. At the microscopic length scale, this behavior can be rationalized by considering the trend of decreasing interaction between liquid and the wall going from the interface to the center of the confinement.

Moreover, the slip velocity is also dependent on the viscosity coefficient of liquid and interfacial friction coefficient between liquid and wall. Therefore, the slip length can be rewritten as,

$$L_s = \frac{\eta}{\lambda} \quad (2.28)$$

where η is the shear viscosity of liquid and λ is the friction coefficient. This relation allows the calculation of slip length in equilibrium because both viscosity and friction coefficient can be calculated via Green-Kubo relation at equilibrium.

Chapter 3

Interfacial Friction Coefficient

3.1 Theory of equilibrium methods

In this Chapter, two equilibrium methods commonly used to compute the friction coefficient are introduced and their assumptions are compared. Results of simulations from equilibrium molecular dynamics and nonequilibrium molecular dynamics are highlighted. In addition, the dependencies of friction coefficient on a variety of parameters are discussed.

3.1.1 Bocquet and Barrat Method

First, we go over a method developed by Bocquet and Barrat[11]. In linear response, slip velocity $\Delta u = u_l - u_s$ is assumed to be linearly related to the velocity of wall, the generalized Langevin equation can then be written as,

$$M \frac{du_s}{dt} = \lambda A \int_0^\infty d\tau \xi(t-\tau) u_s(\tau) + \eta(t) \quad (3.1)$$

where M is the mass of wall, A is the surface area of the wall, ξ is a memory kernel which obeys two nontrivial general relationships. First, because the response of the fluid cannot be instantaneous, $\Delta u = u_s(0^+) - u_l(0^+) = u_s(0^+)$, suggesting the Laplace transform of the memory kernel obeys the sum rule

$$\tilde{\xi}(\omega \rightarrow \infty) = 1 \quad (3.2)$$

Second, classical dynamics must obey Galilean invariance. In this context, the Langevin equation above should not be changed when u_s is changed by a constant, suggesting

$$\tilde{\xi}(\omega = 0) = \int_{-\infty}^\infty \xi(t) dt = 0 \quad (3.3)$$

η is a random force that obeys the fluctuation-dissipation theorem,

$$\langle \eta(0)\eta(t) \rangle = 2\lambda A k_b T \xi(t) \quad (3.4)$$

For any complex number s with $\text{Re}(s) > 0$, the Laplace transform is defined as

$$\tilde{C}(s) = \int_{0^-}^{\infty} dt f(t) \exp[-st] \quad (3.5)$$

Taking the Laplace transform of the velocity autocorrelation function $C(t) = \langle u_s(t)u_s(0) \rangle$, we find

$$\tilde{C}(s) = \frac{k_B T}{M} (s + \alpha \tilde{\xi}(s))^{-1} \quad (3.6)$$

where $\alpha = \frac{\lambda A}{M}$ serves as frequency scale and $C(0) = \frac{k_B T}{M}$ as a consequence of the equipartition theorem. Similarly, the force autocorrelation function,

$$C_{ff}(t) = \langle F(t) \cdot F(0) \rangle = -M^2 \frac{d^2}{dt^2} C(t) \quad (3.7)$$

has a Laplace transform

$$\tilde{C}_{ff}(s) = -M^2 \left(s^2 \tilde{C}(s) - sC(t=0^-) - C'(t=0^-) \right) \quad (3.8)$$

The last term can be rewritten as,

$$C'(t=0^-) = -C'(t=0^+) \quad (3.9)$$

$$= -\lim_{s \rightarrow \infty} s \left[s \tilde{C}(s) - C(t=0) \right] \quad (3.10)$$

$$= \alpha \frac{k_B T}{M} \lim_{s \rightarrow \infty} \frac{s \tilde{\xi}(s)}{s + \alpha \tilde{\xi}(s)} = \alpha \frac{k_B T}{M} \quad (3.11)$$

Where the last step invokes the equation 3.2. Now all the pieces of $\tilde{C}_{ff}(s)$ are known, taking the $s \rightarrow 0$ limit using equation 3.3, we obtain,

$$\tilde{C}_{ff}(s=0) = \lambda A k_B T \lim_{s \rightarrow 0} \left(1 + \frac{s \tilde{\xi}(s)}{s + \alpha \tilde{\xi}(s)} \right) \quad (3.12)$$

$$\lambda = \frac{1}{A k_B T} \int_0^\infty \langle F(t) \cdot F(0) \rangle_0 dt \quad (3.13)$$

$$= \frac{1}{A k_B T} \int_0^\infty C_{ff}(t) dt \quad (3.14)$$

where we find that the friction is given by a Green-Kubo relation, and proportion to the integral of the force-force autocorrelation function.

3.1.2 Hansen method

Hansen considers a slab of liquid near the solid wall in his orginal derivation [12]. For simplicity, the following derivation treats the slab as all liquid that interacts with the solid wall. Consider the solid-liquid shear force F_x that depends on the relative velocity between solid and liquid in

the x direction. If the velocity difference is small, then a linear constitutive equation relating the solid-liquid shear force and the slip velocity $\Delta u = u_l - u_s$,

$$F_x(t) = - \int_0^t \gamma(t-\tau) \Delta u(\tau) d\tau + \eta(t) \quad (3.15)$$

where γ is a friction kernel and η is a random force that also satisfies equation 3.4. If the flow is steady, then in the long time limit

$$\langle F_x \rangle = -\gamma_0 \langle \Delta u \rangle \quad (3.16)$$

where γ_0 is the zero frequency friction coefficient multiplied with the surface area of the wall. For Poiseuille flow, the wall is stationary, so the velocity difference is just the velocity of the liquid, namely $\Delta u = u_l$. Multiplying u_l on both sides and taking the ensemble average, the equation of shear force now becomes an equation relating velocity-force cross correlation function and a velocity autocorrelation function,

$$C_{uF}(t) = \langle u_l(0) F_x(t) \rangle \quad (3.17)$$

$$C_{uu}(t) = \langle u_l(0) u_l(t) \rangle \quad (3.18)$$

$$C_{uF}(t) = - \int_0^t \gamma(t-\tau) C_{uu} d\tau \quad (3.19)$$

Assuming the friction kernel is a sum of exponentially decaying functions,

$$\gamma(t) = \sum_{i=1}^n B_i e^{-D_i t} \quad (3.20)$$

$$\tilde{\gamma}(s) = \sum_{i=1}^n \frac{B_i}{s + D_i} \quad (3.21)$$

where $\tilde{\gamma}$ indicates the Laplace transform of the friction kernel. Take the Laplace transform of relation between C_{uF} and C_{uu} , reorganize to obtain

$$\tilde{C}_{uF}(s) = - \sum_{i=1}^n \frac{\tilde{C}_{uu}(s) B_i}{s + D_i} \quad (3.22)$$

And the zero-frequency friction is then

$$\gamma_0 = \int_0^\infty \sum_{i=1}^n B_i e^{-D_i t} dt \quad (3.23)$$

$$= \sum_{i=1}^n \frac{B_i}{D_i} \quad (3.24)$$

and the intrinsic interfacial friction coefficient λ can be found by dividing γ_0 by the surface area of the confining wall,

$$\lambda = \frac{\gamma_0}{A} \quad (3.25)$$

Now we should consider the discrepancies between the two methods. The physical assumptions in the Barrat and Bocquet method were not considered in the Hansen method. First, consider the response of the fluid,

$$\lim_{s \rightarrow \infty} \sum_{i=1}^n \frac{B_i}{s + D_i} = 0 \quad (3.26)$$

Second, consider Galilean invariance which requires evaluation of the Laplace transform of the memory kernel at the frequency of 0. This is equivalent to find the zero-frequency friction up to a multiplicative factor.

$$\lim_{s \rightarrow 0} \sum_{i=1}^n \frac{B_i}{s + D_i} = \int_{-\infty}^{\infty} \sum_{i=1}^n B_i e^{-D_i t} dt \quad (3.27)$$

$$= \sum_{i=1}^n \frac{B_i}{D_i} \neq 0 \quad (3.28)$$

since B_i and D_i are positive constants.

3.2 Equilibrium simulations and results

3.2.1 Simulation setup

We presented an introduction of the model system before diving deep into the results of friction coefficient. Molecular dynamics simulations were carried out using LAMMPS. A snapshot of the system is captured in Figure 3.1. Liquids are confined within two double-layered graphene walls separated by a distance of $L_y = 2.10, 3.10, 4.10, 5.10$ nm. Periodic boundary conditions were imposed on the x and y directions with simulation domain $L_x = L_z = 3.44$ nm. Interactions between a pair of liquid particles and the interactions between a carbon atom and a liquid particle were modelled by 6-12 Lennard-Jones potential,

$$U_{LJ}(r) = 4\epsilon \left[\left(\frac{\sigma}{r} \right)^{12} - \left(\frac{\sigma}{r} \right)^6 \right]$$

where ϵ and σ serve as the energy and length scales of the fluid. The bulk density of liquid was set to $0.8\sigma^{-3}$ which correspond to 1200 particles when $L_y = 5.10$ nm.

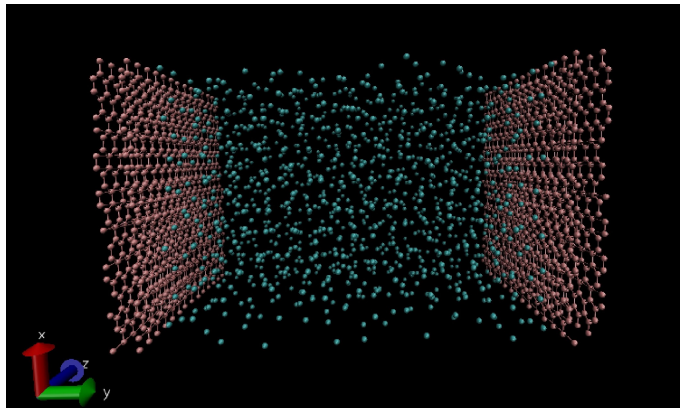


Figure 3.1: A snapshot of simulation in which red spheres represent carbons, red lines correspond to a covalent bond, and blue spheres represent fluid particles and $L_y = 5.10$.

To make the the system more physical, parameters for argon were used and shown in Table 3.1. The interaction between the carbon atoms were modelled by second-generation REBO potential developed by Brenner[13].

A spring constant whose equilibrium distance is the initial position is applied to each carbon atom. Springs were either attached to the initial center of mass of each graphene sheet or attached to the original position of each carbon atom.

The system was equilibrated to 120 K by a Langevin thermostat with $\tau = 0.5$ ps for 5 ns before any statistics were taken.

σ_{ff} (nm)	ϵ_{ff}/k_B (K)	σ_{fw} (nm)	ϵ_{fw}/k_B (K)
0.34	120.0	0.34	57.96

Table 3.1: Parameters for the Lennard-Jones Interaction. f is short for fluid and w is short for wall.

3.2.2 Basic results of the two methods

Here we briefly discuss the applicability of the two methods to our model system. For each side of the wall, the friction along the x-direction can be computed from the sum of all pairwise interactions between the liquid and wall atoms,

$$F_x(t) = \sum_{i \in \text{liquid}} \sum_{j \in \text{wall}} F_{ij,x}(t) \quad (3.29)$$

the friction coefficient along the x-direction can be calculated using equation 3.14,

$$\lambda_x = \frac{1}{Ak_BT} \int_0^\infty \langle F_x(0)F_x(t) \rangle_0 dt = \frac{1}{Ak_BT} \int_0^\infty C_{FF}(t) dt$$

The autocorrelation function and its integration as shown in equation 3.13 are shown in Figure 3.2. The decay time is around 0.5 ps and converges around 4 ps. The large noise of the integrated correlation functions at long time is a consequence of white noise in the decorrelated region.

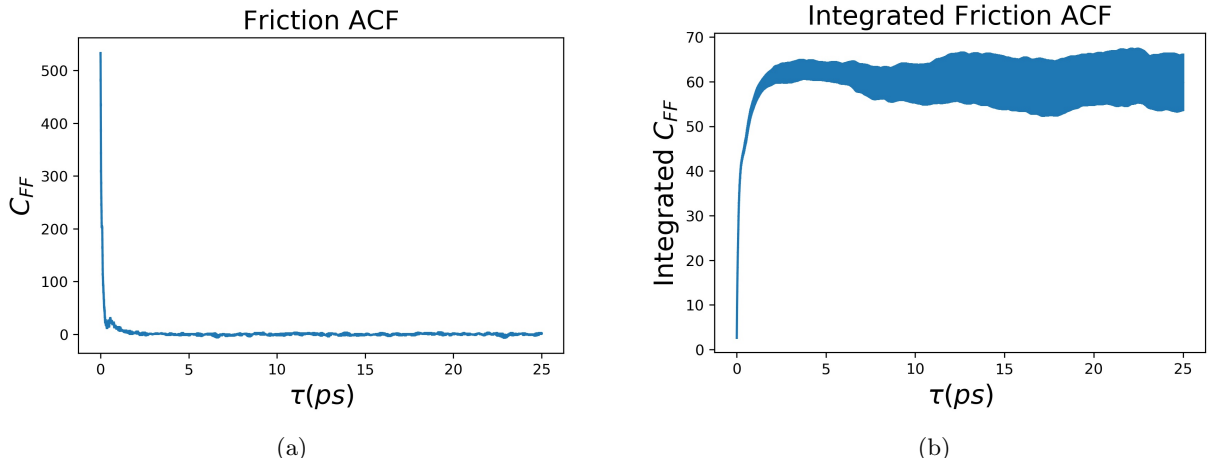


Figure 3.2: (a) Force autocorrelation function. Error bars are too small to be observed (b) Integrated Force autocorrelation function. The shaded area corresponds to 1 standard error obtained from block averaging.

Now consider the Hansen method. The correlation functions and their Laplace transform as defined in equations 3.17, 3.18 and 3.22 are shown in Figure 3.3. The decay time for $C_{uu}(t)$ is

around 2 ps and does not converge even after 30 ps. The $C_{uf}(t)$ function is extremely noisy so a Savitzky–Golay filter was applied[14]. Force and velocity are uncorrelated at time $t = 0$ because force is only a function of position. Then there is a recoil because the direction of friction is in the opposite direction of motion.

In Laplace space, \tilde{C}_{uu} never converges. Moreover, finding appropriate parameters to describe \tilde{C}_{uf} is very difficult and error-prone at low frequency, demonstrated by the large deviations of the red squares from green dots. Because Hansen’s method is heavily dependent on post-processing, the method is not numerically robust.

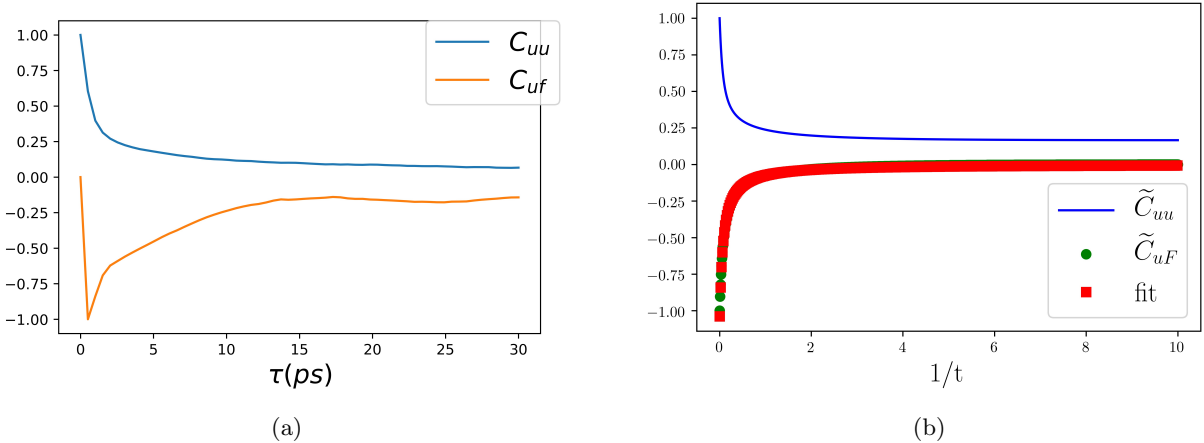


Figure 3.3: (a) The liquid velocity autocorrelation function in blue and liquid velocity friction cross correlation function in orange. High frequency information in C_{uf} has been filtered. (b) The correlation functions in Laplace space.

Overall, the BB method is more straightforward and robust. Therefore, The following part of this thesis employs the BB method to investigate interfacial friction coefficients.

3.2.3 Dependence of friction coefficient on wall thermostat

The underdamped Langevin equation was discussed in Chapter 2.1.2. The coupling strength between the particle and the bath is determined by the damping time $\tau = \frac{m}{\gamma}$. The smaller the damping time, the stronger the interaction.

In BB formulation, friction coefficient is independent of the damping time of wall. However, in practice, due to the constrain of finite time sampling, the damping time may affect the extent of the interaction between wall and liquid. For example, if the wall particles are very damped, the rate of change energy becoming very fast, modifying the motions significantly. The dependence of friction on the damping time of wall thermostating is plotted in Figure 3.4.

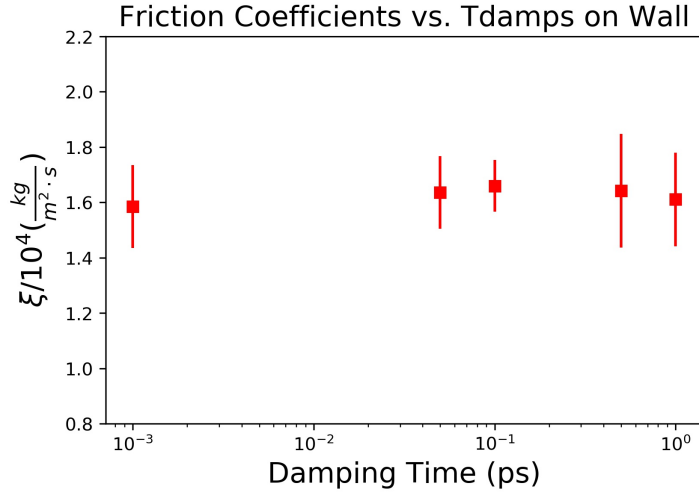


Figure 3.4: The damping times considered were 1, 50, 100, 500, 1000 femtoseconds.

which demonstrates that the motion of the wall is sufficiently decoupled from the force-force correlation function.

3.2.4 Dependence of friction coefficient on sheet flexibility

Tuning the stiffness constant changes the flexibility of the graphene sheet. Moreover, fixing the spring to the center of mass of the whole sheet makes the sheet more flexible comparing to fixing the spring to the center of mass of each carbon atom. For the former, stiffness = 0.02, 0.2, 2 $\frac{eV}{\text{\AA}^2}$ were considered. For the latter, stiffness = 15 $\frac{eV}{\text{\AA}^2}$ was considered. The results are summarized in Figure 3.5.

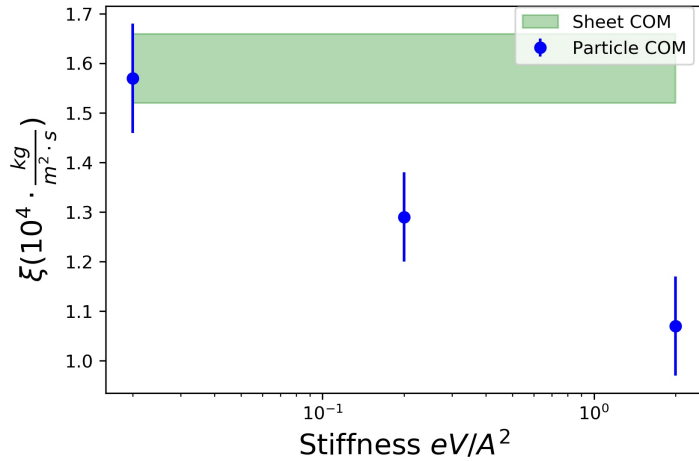


Figure 3.5: The blue dots correspond to results from simulations where the center of mass of each carbon atom is fixed. For the green shade, center of mass of each sheet is fixed.

As a sheet becomes more flexible, the fluctuations in its positions also increase, leading to an

increase in the interactions between wall and liquid which is equivalent to an jump in friction.

3.2.5 Dependence of friction coefficient on slab width

A slab is a chunk of liquid near the wall, and slab width is distance from the wall to the end of the slab. At the interface, liquid becomes layered as seen in a solvation shell because of the attractions between liquid and solid. It was hypothesized that only the first layer contains information of the intrinsic friction as subsequent layers are influenced by viscous force of liquid[15]. Nevertheless, such hypothesis is not very general so actual dependence is related strongly to the form of inter-atomic potential. Friction coefficients for $L_y = 5.1 \text{ nm}$ system were calculated at different slab widths; the results are plotted in Figure 3.6.

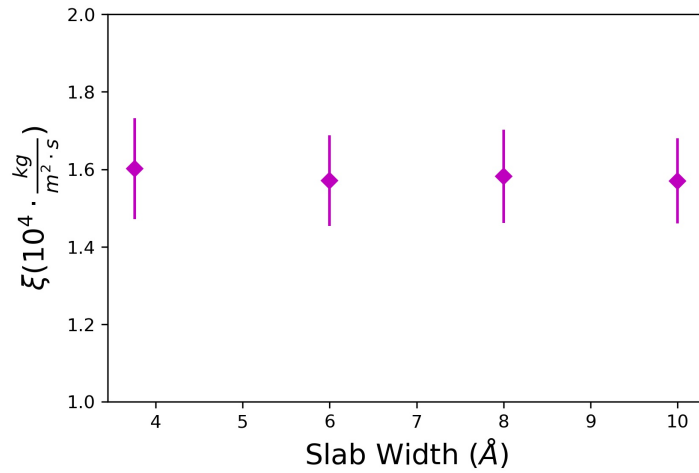


Figure 3.6: The slab widths were selected to be 3.76, 6, 8, 10 Å which respectively contains 1, 2, 3 or 4 layers of liquid.

The results suggest there is no dependence of friction coefficients on slab widths for our model system in contrast to calculation using the Hansen method. The lack of dependence may arise from two reasons. First, the interactions among argon are stronger than the interaction between argon and carbon so the layers can exchange particles faster than the friction autocorrelation relaxes. Second, argon is a fairly viscous liquid so viscous force is significant enough to affect the first layer, and cannot be separated from intrinsic interfacial friction.

3.2.6 Dependence of friction coefficient on length of wall

Finite size effects has an important role for physical properties when the system size is on the order of nanometer. Finite size effect can arise when the length of the wall is changed. As the surface of area of the graphene sheets becomes smaller, the extent of position fluctuation along the horizontal axis becomes more pronounced, leading to an increase of friction coefficient. This extent

may be further magnified at small slab widths. Indeed, this is found in calculations performed for various wall domains shown in Figure 3.7.

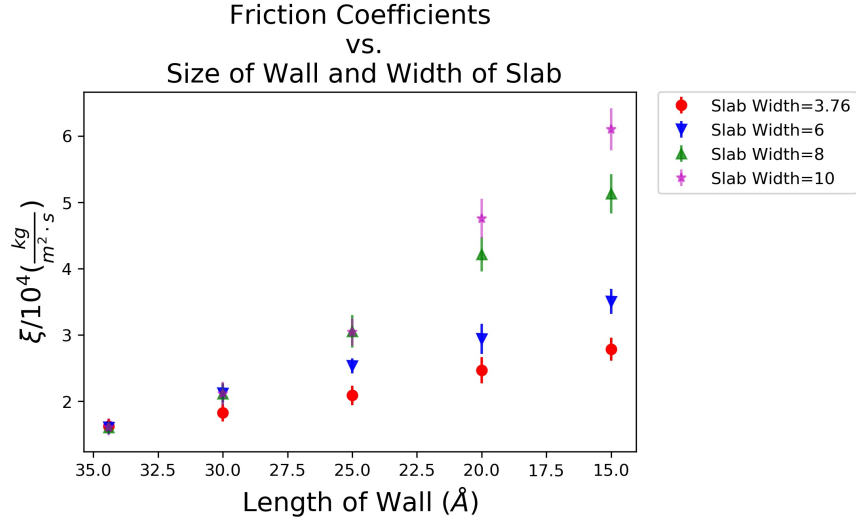


Figure 3.7: Each type of marker correspond to a slab width in Å.

3.2.7 Dependence of friction coefficient on channel width

Another finite size effect arises by limiting the space within confinement. Previous researches have shown that this scaling of friction coefficient is strongly subject to the geometries of confinement and the shapes of the liquid molecules. For water within carbon nanosheets, it was observed that the interfacial friction coefficient is not affected by the channel width. However, for water flow within a nanotube, friction decreases as radius decreases[7]. The results from our simulations are shown in Figure 3.8.

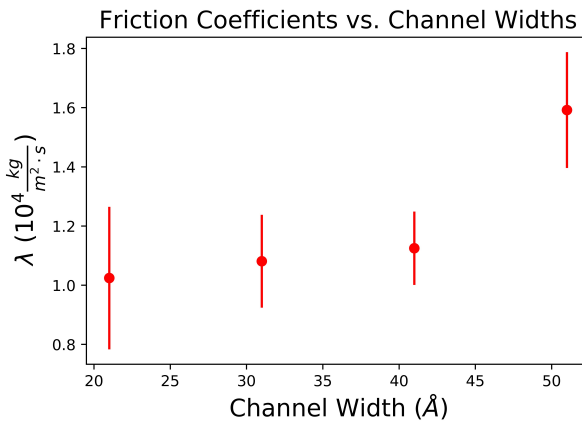


Figure 3.8: The channel widths were selected to be 21, 31, 41, 51 Å.

3.3 Nonequilibrium simulations and results

For the nonequilibrium simulation, equilibrium configuration were generated using procedures as discussed in Section 3.2.1. In addition, a constant external force is applied to the liquid particles along the x-direction to imitate a Poiseuille flow; the driven acceleration was $3 \times 10^{10} \frac{m}{s^2}$. At steady state, the liquid particles should have a distinct velocity and density profiles. The time to reach steady state for this system was around 10 ns.

3.3.1 Density profiles

Density profiles provide a rudimentary check of validity of simulations; these profiles are presented in Figure 3.9.

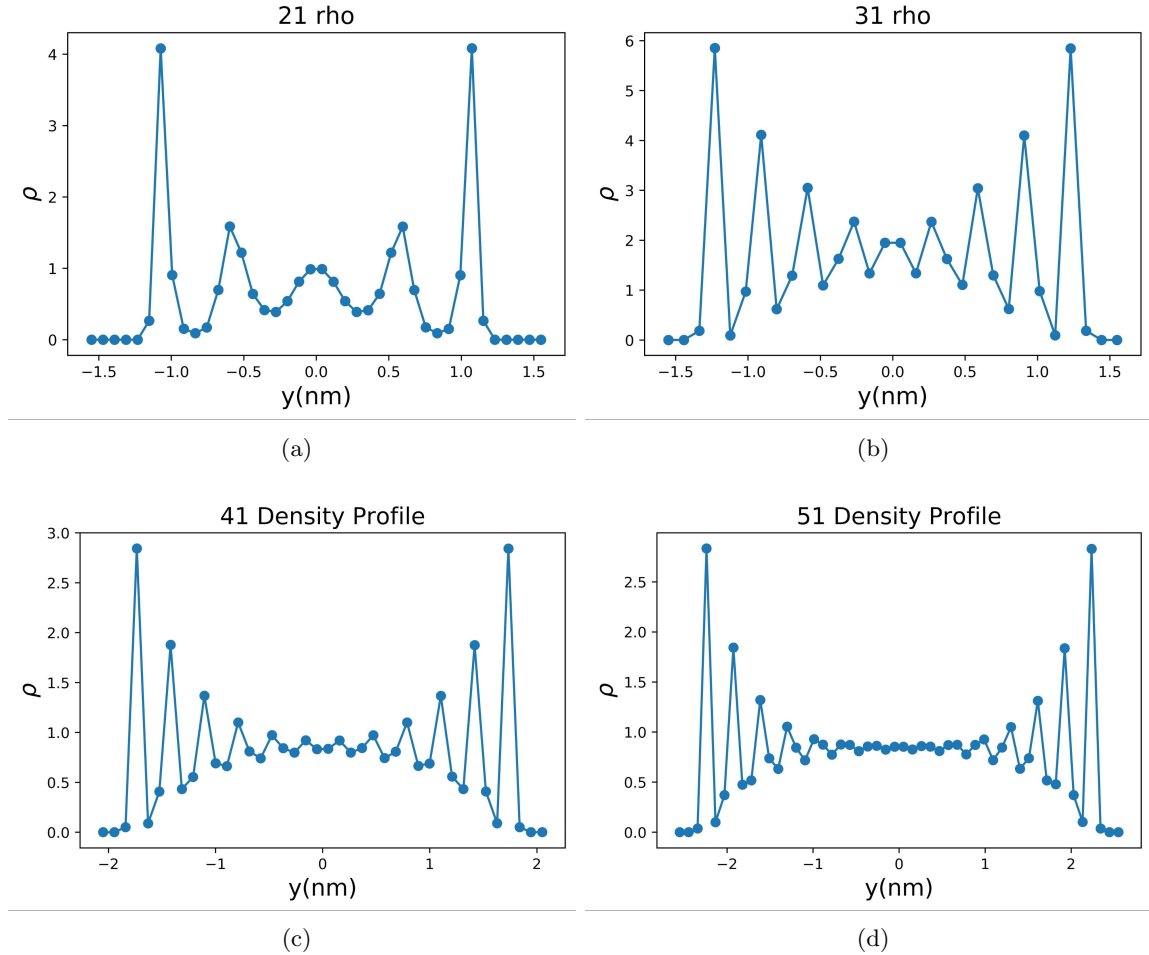


Figure 3.9: (a)(b)(c)(d) Number density profiles of nonequilibrium system at $L_y = 2.1, 3.1, 4.1$, and 5.1 nm .

As the channel width shrinks, bulk liquid in the middle gradually disappears and the layered features of liquid near the interface becomes more predominant.

3.3.2 Velocity profiles

The velocity of the first solvation shell was used as the slip velocity. The strain rate at the wall was calculated using a parabolic fit as shown in equation 2.26. reference viscosity coefficient of liquid, $\eta = 1.62 \pm 0.04 \cdot 10^{-4} \frac{kg}{m \cdot s}$ was used to connect slip length and friction coefficient[16]. The results are plotted in Figure 3.10.

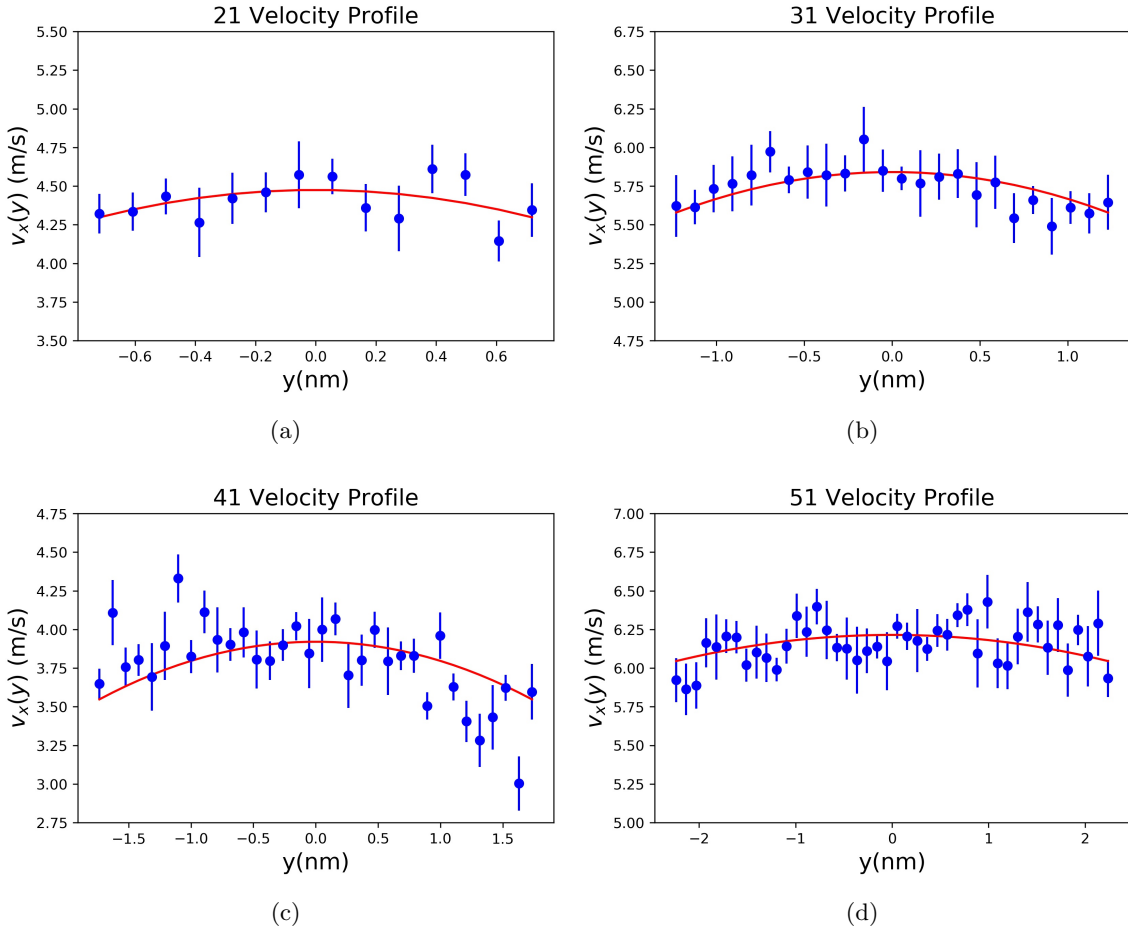


Figure 3.10: (a)(b)(c)(d) u_x profiles of nonequilibrium system at $L_y = 2.1, 3.1, 4.1$, and 5.1 nm. The red lines are parabolic least squared regression fit.

3.3.3 Dependence on channel width

A velocity profile can be used to calculate friction coefficients by equation 2.25. Friction coefficients obtained from nonequilibrium simulations were compared their equilibrium counterparts, the results are summarized in Figure 3.11.

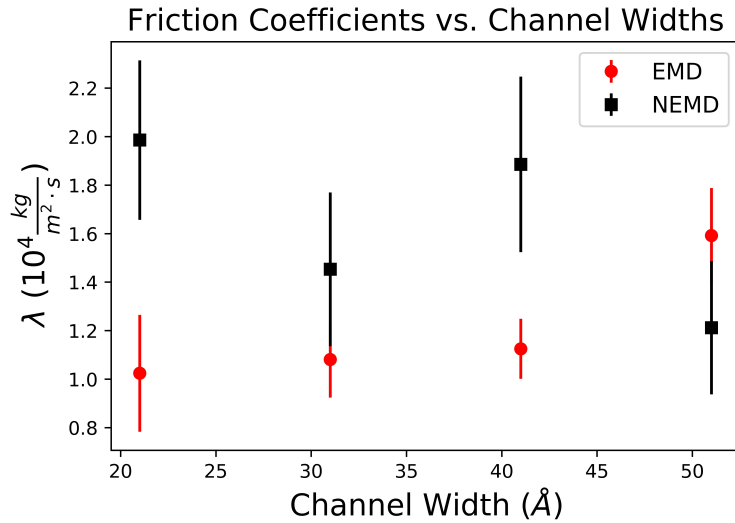


Figure 3.11: The channel widths were selected to be 21, 31, 41, 51 Å.

NEMD and EMD results agreed weakly. NEMD results have high variances because the disappearance of bulk liquid obstructs the fitting of velocity profiles. Moreover, the viscosity coefficient was calculated for bulk system and may not be sufficient when boundary effects are strong. Both EMD and NEMD suggest that the interfacial friction coefficient is relatively unchanged with respect to change in channel width for our model system.

Chapter 4

Heat Transfer Coefficient

In this chapter, equilibrium and nonequilibrium methods to obtain heat transfer coefficient are discussed. Moreover, the connection between friction and heat transfer are studied through the formalism of Onsager reciprocal relations.

4.1 Equilibrium methods and results

Now, consider the heat transfer coefficient κ . A heat current J is defined as

$$\frac{dQ}{dt} \equiv J = \sum_i E_i v_i - S_i v_i \quad (4.1)$$

where E_i is the energy of atom i , v_i is the velocity of atom i and S_i is the stress tensor. And κ can be obtained via a similar Green-Kubo relation as shown in equation 2.23,

$$\kappa = \frac{1}{V k_B T^2} \int_0^\infty \langle J(0) \cdot J(t) \rangle_0 dt \quad (4.2)$$

Because the autocorrelation function involves a dot product, transport coefficients along different directions can be obtained independently by only considering current along that direction. The heat transfer is equal to the energy changed by the Langevin thermostat and the heat current is $J = \frac{\Delta Q}{\Delta t}$; $L_y = 5.1 nm$ was used. The integrated correlation functions are presented in Figure 4.1. Decay time along the x-axis is about one order of magnitude higher than the decay time along the y-axis. Moreover, $\kappa_x > \kappa_y$ agrees with the fact that graphene is better at transferring heat in-plane instead of out-of-plane.

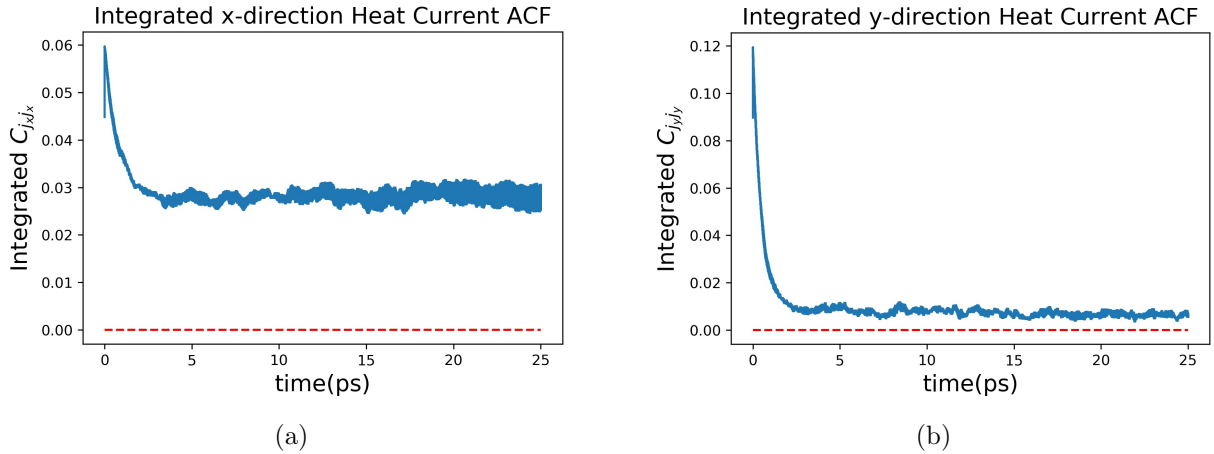


Figure 4.1: (a)(b) Integrated heat current autocorrelation function for x and y directions respectively. The shaded area corresponds to one standard error. The red dashed line is zero to help observe that autocorrelation function does not decay to 0.

After unit conversion, we found $\kappa_x = 42 \pm 4.6 \frac{W}{m \cdot K}$ and $\kappa_y = 5.1 \pm 0.4 \frac{W}{m \cdot K}$. Because heat transfer is hugely dependent on the type of interaction potential used, no literature comparison exists. Nevertheless, the result appears reasonable because κ 's are few order of magnitudes higher than the heat conductivity of bulk argon and a few order of magnitudes lower than the heat conductivity of graphene.

4.2 Nonequilibrium methods and results

A temperature gradient can be imposed across the carbon nanochannels to understand how heat is transferred from one graphene wall to the other graphene wall through a medium of argon liquid. At steady state, a steady heat current should be observed from the source to sink. In the linear response regime, the perturbation to the Hamiltonian arises from inverse temperature. In this, the heat transfer coefficient is defined as

$$Q = \kappa t \Delta T \quad (4.3)$$

where t is time and ΔT is the temperature gradient. The temperature profiles for system with $L_y = 2.1\text{ nm}$ and $L_y = 5.1\text{ nm}$ are plotted in Figure 4.2 and the temperature gradient was 20 K.

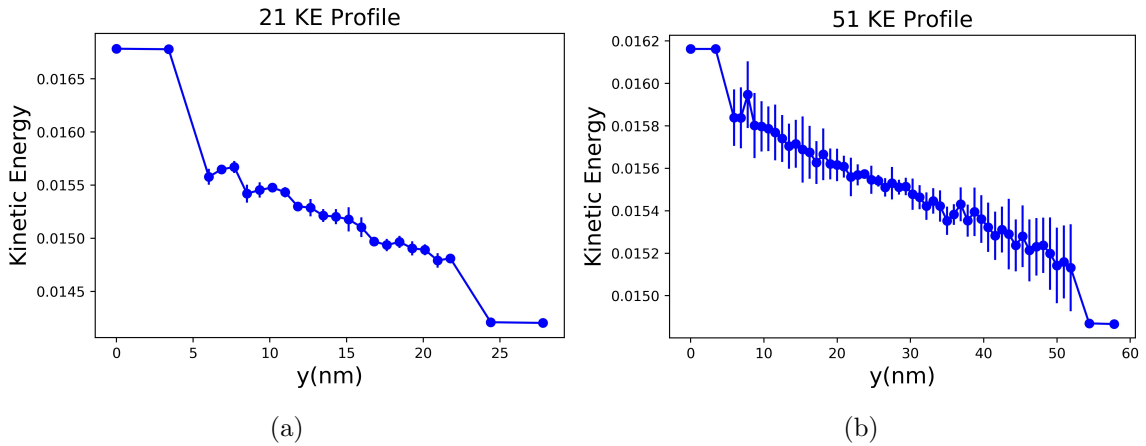


Figure 4.2: (a)(b)The kinetic energy profile. The leftmost two and the rightmost two points correspond to graphene heat reservoir and heat sink. Remaining points correspond to argon.

In the linear response regime, the temperature profile through the liquid should be linear. The temperature difference across both boundaries should be the same when boundary effects are not strong; this was achieved when $L_y = 5.1\text{ nm}$ but not when $L_y = 2.1\text{ nm}$. This method is often difficult because choosing appropriate temperatures on the boundary requires trials and errors. If the temperature difference between the two walls is too large, the system is not in the linear response regime. If the temperature difference between the two walls is too small, statistical noise would be indistinguishable from temperature gradient.

4.3 Correlation between friction and heat current

4.3.1 Onsager reciprocal relation

First, let us recap the general relation shown in Landau's book[17]. Consider macroscopic quantities $x_1 \dots x_N$ that deviate slightly from equilibrium; in other words, the perturbation is in the linear response regime. Assume $\langle x_i \rangle = 0$ at equilibrium, and x_i 's is invariant under time reversal

$$\dot{x}_i = - \sum_j \lambda_{ij} x_j \quad (4.4)$$

where λ_{ij} denotes the ij entry of the matrix $\boldsymbol{\lambda}$ which describes time-dependent response of x_i given a deviation of x_j . Now consider the conjugate quantity of x_i ,

$$X_i = - \frac{\partial S}{\partial x_i} \quad (4.5)$$

where S is entropy and X_i are generalized forces. In the linear response regime,

$$X_i = \sum_j \beta_{ij} x_j \quad (4.6)$$

$$\beta_{ij} = - \frac{\partial X_i}{\partial x_j} \quad (4.7)$$

Moreover, β_{ij} are clearly the second derivative of S , and therefore

$$\beta_{ik} = \beta_{ki} \quad (4.8)$$

Now equation 1 can be rewritten using equation 4.6,

$$\dot{x}_i = - \sum_j \gamma_{ij} X_j \quad (4.9)$$

$$\gamma_{ij} = \frac{\lambda_{ij}}{\beta_{ij}} \quad (4.10)$$

where $\boldsymbol{\gamma}$ is the matrix of kinetic coefficients.

Now consider how x_i 's are connected in time through a time correlation function,

$$\langle x_i(t) x_j(0) \rangle = \langle x_i(0) x_j(t) \rangle \quad (4.11)$$

the equality holds due the time reversal symmetry of equilibrium fluctuation. Differentiate both sides with respect to time using equation 6, and set time to $t = 0$

$$\sum_j \gamma_{ij} \langle X_j x_j \rangle = \sum_i \gamma_{ji} \langle x_i X_i \rangle \quad (4.12)$$

Now calculate the average,

$$\langle X_i x_j \rangle = - \int d\mathbf{x} e^{S[\mathbf{x}]} \frac{\partial S}{\partial x_i} x_j \quad (4.13)$$

$$= - \int d\mathbf{x} \frac{\partial}{\partial x_i} (e^{S[\mathbf{x}]}) x_j \quad (4.14)$$

$$= \int (e^{S[\mathbf{x}]}) \frac{\partial x_j}{\partial x_i} = \delta_{ij} \quad (4.15)$$

For simplicity, restrict our focus on a pair of quantities i and j . Substitute back into equation 4.12, we arrive at the Onsager reciprocal relation.

$$\gamma_{ij} = \gamma_{ji} \quad (4.16)$$

as expected.

In this thesis, we consider how heat transfer and friction are correlated in the linear response regime through a 2x2 Onsager phenomenological matrix. The diagonal elements are commonly encountered transport coefficients and the off-diagonal elements are the kinetic coefficients connecting friction and heat transfer. The off diagonal elements can be quantified through a cross correlation functions of the currents. The matrix is

$$\mathbf{M} = \begin{bmatrix} \lambda & \gamma_{FJ} \\ \gamma_{JF} & \kappa \end{bmatrix} \quad (4.17)$$

$$= \begin{bmatrix} \frac{1}{Ak_B T} \int_0^\infty \langle F(0) \cdot F(t) \rangle_0 dt & \int_0^\infty \langle F(0) J(t) \rangle_0 dt \\ \int_0^\infty \langle J(0) F(t) \rangle_0 dt & \frac{1}{V k_B T^2} \int_0^\infty \langle J(0) \cdot J(t) \rangle_0 dt \end{bmatrix} \quad (4.18)$$

where λ is interfacial friction coefficients (not to be confused with matrix elements in equation 4.4). κ is heat transfer coefficient. F is friction and J is heat current.

At this point, diagonal elements have been calculated and understood, so the remaining of this chapter is dedicated to the calculation of the off-diagonal elements. Similar to a Green-Kubo relation, the response of heat generation due to friction or vice versa can be captured by a cross-correlation function,

$$R_{JF}(t) = \int_0^\infty \langle J(0) F(t) \rangle_0 dt = \int_0^\infty C_{JF}(t) dt \quad (4.19)$$

Moreover,

$$R_{JF}(t) = R_{FJ}(t)$$

which directly follows from Onsager's reciprocal relations.

Now consider the behavior of $C_{JF}(t)$. A time $t = 0$, since the liquid particles have not affected the wall at all, no correlation is expected,

$$C_{JF}(0) = 0 \quad (4.20)$$

Then liquid particles come into contact with wall, a process that transfers kinetic energy, consequently inducing the wall to dissipate energy into bath. So at short time, $C_{JF} > 0$. In the long time limit, it is reasonable to assume the two currents have decorrelated,

$$C_{JF}(\infty) = \langle J(0) \rangle_0 \langle F(\infty) \rangle_0 = \langle J(0) \rangle_0 \langle F(0) \rangle_0 = 0 \quad (4.21)$$

following the stationarity of equilibrium.

Despite the fact that cross-correlation functions are easy to compute, the numerical result often suffers from significant noise. Therefore, an non-equilibrium simulation may also be used. In this report, we focus on the model of plane Poiseuille flow in which a pressure difference ΔP induces a driven force. At steady state, liquid particles are transferred through confinement steadily and have a non-zero net frictional interactions with the wall in the direction of flow. In the language of Onsager reciprocal relations, external force plays the role of a generalized force and current of interest is the rate of heat transfer. Define:

$$J = -\gamma_{FJ} F_e \quad (4.22)$$

Then, the steady-state heat dissipation can be analyzed to understand how friction induces heat transfer. Equivalently, how a temperature gradient causes momentum transfer can also be analyzed.

4.3.2 Cross correlation functions

The integrated cross correlation function between friction and heat current along the x direction is shown in Figure 4.3.

At short time $\int_0^t C_{JF}(t)$ is positive, agrees with our intuition. Because friction generates heat and the decay time scales for friction and heat current are on the same order of magnitude, the cross correlation is expected to decorrelate in a similar rate; unfortunately, this behavior was not observed due to noisy data.

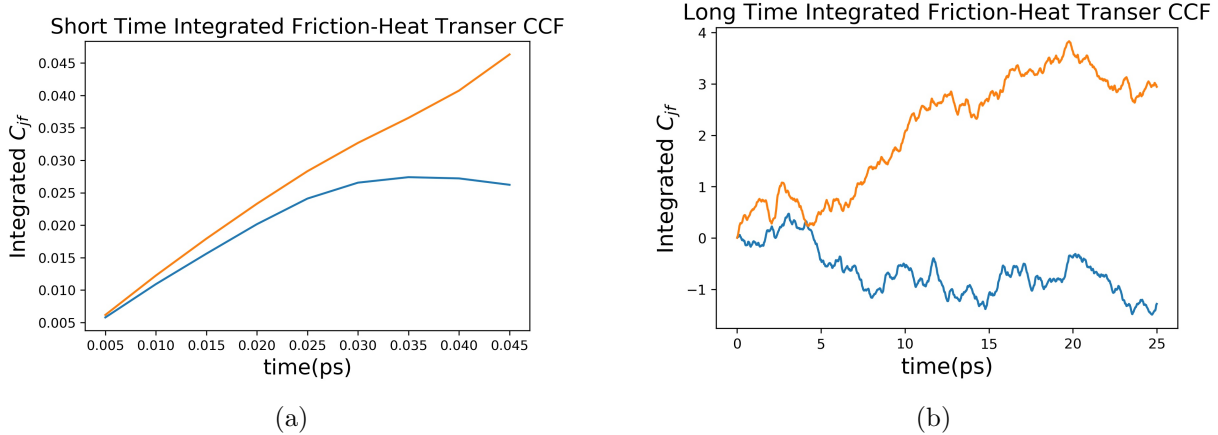


Figure 4.3: (a)(b) Integrated friction and heat current cross correlation function at short time and at long time. Each line represents one block average over 10 ns.

4.3.3 Heat generated from channel flow

The energy dissipated into the bath as a function of time for one side of the graphene nanochannels is shown in Figure 4.4. The negative sign indicates bath removes energy from graphene walls. The driven acceleration on the liquid particles was $1 \cdot 10^{11} \frac{m^2}{s}$. The average rate of heat transfer can be obtained by performing a linear fit. Then γ_{FJ} can be calculated by equation 4.23. And we have $\gamma_{FJ} = 1.67 \cdot 10^{-21} \frac{kg \cdot m}{s}$. The physicality of this result remains to be verified.

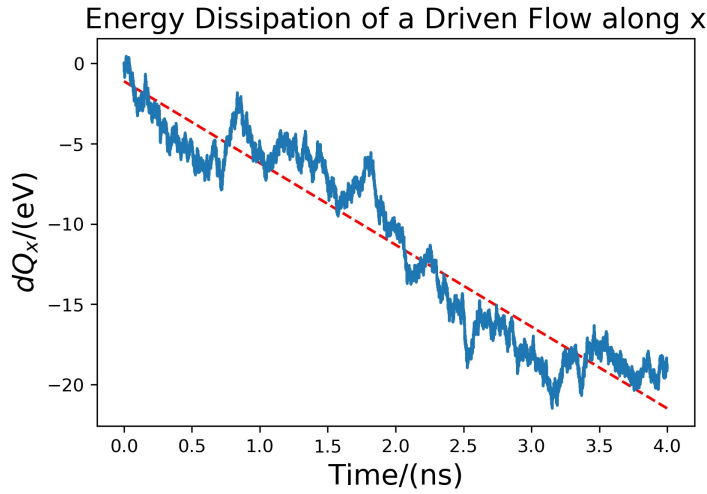


Figure 4.4: The energy dissipation by a graphene wall in a Poiseuille flow along the x direction. The blue line is the exact energy released and the red dashed line is the linear least squared regression fit.

Conclusion and Outlooks

In this thesis, matrix elements of an Onsager matrix describing friction and heat transfer in a model system of argon confined within graphene nanochannels were calculated by equilibrium and nonequilibrium molecular dynamics. The results of diagonal elements agreed with previous literature and captures the qualitative behavior of experimental observation. The calculation of the off diagonal elements can serve as starting point to understand the complication of heat dissipation in microfluidic devices.

In the future, a more careful and analytic argument should be developed to prove the off diagonal elements are positive. Moreover, the Onsager matrix should also be studied for confinements with different geometry.

Bibliography

- [1] Geim, A. K.; Novoselov, K. S. The rise of graphene. *Nature Materials* **2007**, 6, 183-191.
- [2] Das, T. et al. Graphene-based flexible and wearable electronics. *Journal of Semiconductors* **2018**, 39, 1.
- [3] Boretti, A. et al. Outlook for graphene-based desalination membranes. *npj Clean Water* **2018**, 1(5).
- [4] Liu, J.; Cui, L.; Losic, D. Graphene and graphene oxide as new nanocarriers for drug delivery applications. *Acta Biomaterialia* **2013**, 9(12), 9243-9257.
- [5] Xie, Q. et.al. Fast water transport in graphene nanofluidic channels. *Nature Nanotechnology* **2018**, 13, 238–245.
- [6] Priezjev, N. V. Molecular diffusion and slip boundary conditions at smooth surfaces with periodic and random nanoscale textures. *J. Chem. Phys* **2007** 127, 144708.
- [7] Falk, K. et.al. Molecular origin of fast water transport in carbon nanotube membranes: superlubricity versus curvature dependent friction. *Nano Letters* **2010**, 10, 4067-4073.
- [8] Pop, E.; Varshney, V.; Roy, A. K. Thermal properties of graphene: Fundamentals and applications. *MRS Bulletin* **2012**, 37 (12), 1273–1281.
- [9] Limmer, T. D.; Chloe, Y. G. *Chemistry 220B Lecture Notes*; University of California at Berkeley: Berkeley, CA, 2019.
- [10] Gallavotti, G. *Nonequilibrium and Irreversibility*; Springer:Berlin, 2014
- [11] Bocquet, L.; Barrat J. L. On the Green-Kubo relationship for the liquid-solid friction coefficient. *J. Chem. Phys* **2013**, 139, 044704.
- [12] Kannam, S. K. et al. Slip flow in graphene nanochannels. *J. Chem. Phys* **2011**, 135, 144701.
- [13] Brenner, D. W. et al. A second-generation reactive empirical bond order (REBO) potential energy expression for hydrocarbons. *J. Phys.: Condens. Matter* **2002**, 14, 783.
- [14] Savitzky, A. Golay, M. J. E. Smoothing and differentiation of data by simplified least squares procedures. *Anal. Chem.* **1964**, 36 (8), pp 1627–1639.
- [15] Hansen, J. S.; Todd, B. D.; Davis, P. J. Prediction of fluid velocity flip at solid surfaces. *Physical Review E* **2011**, 84, 016313
- [16] Rowley, R. L.; Painter, M. M. Diffusion and viscosity equations of state for a Lennard-Jones fluid obtained from molecular dynamics simulations. *International Journal of Thermophysics* **1997**, 18, 5, 1109-1121.
- [17] Landau, L. D.; Lifshitz, E.M. *Statistical Physics, Part 1*. Oxford, UK, 1975, pp 365-367.